

Cooler and drier climate in the South–Central Pacific during the last glacial period

Received: 16 January 2025

Accepted: 20 February 2026

Cite this article as: Peuple, M.D., Skinner, D.T., Inglis, G.N. *et al.* Cooler and drier climate in the South–Central Pacific during the last glacial period. *Commun Earth Environ* (2026). <https://doi.org/10.1038/s43247-026-03356-8>

Mark D. Peuple, Daniel T. Skinner, Gordon N. Inglis, Manoj Joshi, Peter Langdon, Adrian J. Matthews, Timothy J. Osborn, Rob Scaife, Jean-Yves Meyer & David Sear

We are providing an unedited version of this manuscript to give early access to its findings. Before final publication, the manuscript will undergo further editing. Please note there may be errors present which affect the content, and all legal disclaimers apply.

If this paper is publishing under a Transparent Peer Review model then Peer Review reports will publish with the final article.

Cooler and drier climate in the South–Central Pacific during the last glacial period

Mark Peuple^{a*}, Daniel T. Skinner^{b,c,g}, Gordon N. Inglis^d, Manoj Joshi^{b,c},
Peter Langdon^a, Adrian J. Matthews^{c,e}, Timothy J. Osborn^{b,c}, Rob Scaife^a,
Jean-Yves Meyer^f, David Sear^a

^aSchool of Geography and Environmental Science, University of Southampton,
University Road, Southampton, SO17 1BJ, UK.

^bClimatic Research Unit, University of East Anglia, Norwich, NR4 7TJ, UK.

^cSchool of Environmental Sciences, University of East Anglia, Norwich, NR4 7TJ, UK.

^dSchool of Ocean and Earth Science, University of Southampton, European Way,
Southampton, SO14 3ZH, UK.

^eSchool of Engineering, Mathematics and Physics, University of East Anglia,
Norwich, NR4 7TJ, UK.

^fDélégation à la Recherche, Tahiti, 98713 Papeete, French Polynesia.

^gSchool of Geographical Sciences, University of Bristol, University Road, Bristol, BS8
1SS, UK.

*Corresponding author(s). E-mail(s): M.D.Peuple@soton.ac.uk;

Abstract

Understanding how precipitation responds to temperature change is crucial for anticipating future climate variability. The geological past provides a unique window into rainfall responses to large-scale climate shifts, yet regional responses in the South–Central Pacific remain poorly constrained due to the lack of continuous long-term palaeoclimate records extending beyond the Holocene. To address this gap, we reconstruct temperature and precipitation using biomarker proxies from a 50,000-year peat core from Nuku Hiva, French Polynesia. During the Last Glacial period, increased hydrogen isotopic values of plant waxes indicate drier conditions. Pollen data show increased abundances of drought-adapted herbaceous taxa and reduced cloud forest species. Temperature-sensitive bacterial lipids indicate substantially cooler glacial conditions relative to the Holocene. Notably, reconstructed temperature and precipitation changes are strongly correlated, consistent with data assimilation studies. These results highlight the sensitivity of the tropical Pacific to background climate state and provide important constraints on regional climate dynamics.

Keywords: Last Glacial Period, South Pacific Convergence Zone, Hydroclimate

Main

The South Pacific Convergence Zone (SPCZ) is the principal rain source for over 10 million people in the South–Central Pacific¹. Formed by the convergence of low-level westerly and trade winds² the SPCZ is a diagonally-oriented zone of intense precipitation and cyclogenesis³. The location and strength of the SPCZ changes with El Niño Southern Oscillation (ENSO) cyclicity, with El Niño periods seeing wetter conditions and La Niña periods seeing drier periods^{4;5}. During a strong El Niño event, the SPCZ can adopt a zonal configuration whereby its meridional tilt collapses, triggered by a marked decrease in trade wind strength^{6;7}. These events expose northern and eastern island communities to extreme rainfall events³ (Fig. S1) which strongly impact local agriculture⁸. Conversely, during strong La Niña, the SPCZ moves south, causing droughts which have led to the deaths of thousands of inhabitants of island communities⁸ in the northern SPCZ region.

Palaeoclimate studies have indicated that ENSO and the closely related Pacific Decadal Oscillation (PDO) cycles were the principal modes of variation in the SPCZ over the past 400 years^{9–12}. In the context of such palaeoclimate studies, where proxy records often integrate climate information over several decades or centuries, long-term shifts in the mean state of the Pacific are often referred to as ‘El Niño-like’ or ‘La Niña-like’ conditions to distinguish them from individual, inter-annual events. How the SPCZ will respond to future changes, however, is uncertain¹³, with different groups of models indicating that the SPCZ will remain the same^{14;15}, become more zonal^{6;14;15} or shift to the south^{14;15}. Part of this uncertainty is caused by model sea surface temperature (SST) biases, preventing an accurate simulation of the modern SPCZ location⁵, and in part arises from significant model uncertainty in the precipitation response in a warmer world¹⁶. Additionally, we have limited knowledge of how the SPCZ responds to different (past or future) climate regimes.

Reconstructing the hydroclimate response to different temperature regimes, such as the Last Glacial Period, can provide information about regional climate regimes. However, a critical gap remains in our knowledge of precipitation patterns during the Last Glacial Period, especially in regions like the South–Central Pacific (Fig. 1a), where geographical isolation creates difficulty in identifying glacial age sediments from which to extract palaeoclimate information. Addressing this gap in knowledge is essential for improving future projections of climate dynamics in this remote, under-studied and globally significant region (Fig. 1a). In this study, we extend our knowledge of the South Pacific’s climate history from the previously studied 2.5 ka^{12;17–19} by presenting the first biomarker and pollen-based precipitation and temperature reconstruction covering an extended period to 50 ka. Specifically, we measure the hydrogen isotopic composition of plant wax biomarkers ($\delta^2\text{H}_{\text{wax}}$) from peat core sediments to constrain past changes in precipitation strength from Nuku Hiva, a 4.8–3.6 Ma-old basaltic island in the Marquesas archipelago, French Polynesia (Fig. 1a–b).

We also measure pollen composition down-core, which acts as an independent qualitative proxy for precipitation and temperature. To quantify changes in temperature we measure branched glycerol dialkyl glycerol tetraether (brGDGTs), which are bacterial membrane lipids whose distributions are sensitive to changes in air temperature. Our multi-proxy reconstruction allows us to provide crucial information on the sensitivity of precipitation to changes in local temperature in this critically understudied part of the world.

$\delta^2\text{H}_{\text{wax}}$ and pollen precipitation reconstruction

The hydrogen isotopic composition of plant waxes ($\delta^2\text{H}_{\text{wax}}$) correlates linearly with the hydrogen isotopic composition of precipitation ($\delta^2\text{H}_{\text{precip}}$)^{22–24}, allowing $\delta^2\text{H}_{\text{wax}}$ to serve as a proxy for precipitation intensity in the SPCZ region, where higher rainout produces more negative $\delta^2\text{H}_{\text{wax}}$ values²⁵. To estimate precipitation isotopes, we convert $\delta^2\text{H}_{\text{wax}}$ to $\delta^2\text{H}_{\text{precip}}$ using a dynamic apparent fractionation factor (ϵ_{lw}). This factor was calculated for each sample based on its pollen assemblage, assigning literature-derived ϵ_{lw} values to our main plant functional types: trees²⁶, herbs²², and ferns²⁷. This accounts for vegetation-induced changes in hydrogen isotopic fractionation through time, consistent with established theoretical and empirical frameworks^{28–30}. We also applied a correction for the change in mean ocean hydrogen isotopic composition during the last glacial period based on a global benthic $\delta^{18}\text{O}$ stack³¹. Changes in ocean temperature can alter the isotopic composition of the moisture source and local sea surface temperature reconstruction indicates that the LGM experienced a 2°C decrease in temperature relative to modern, which would have caused a 2‰ decrease in $\delta^2\text{H}_{\text{precip}}$. Changes in humidity may have altered leaf water evapotranspiration and thus $\delta^2\text{H}_{\text{wax}}$, but this effect would lead to an apparent strengthening of the relationship between modelled $\delta^2\text{H}_{\text{precip}}$ and precipitation amount³². Our new $\delta^2\text{H}_{\text{precip}}$ reconstruction reveals major hydrological shifts over the past 50 ka. Specifically, $\delta^2\text{H}_{\text{precip}}$ increased 15‰ during the Last Glacial Maximum (LGM; Fig. 2c) compared to the late Holocene, suggesting a decrease in precipitation relative to present. In contrast, the late- to mid-Holocene appears wetter than the preindustrial period, with $\delta^2\text{H}_{\text{precip}}$ values approximately 20‰ lower than the early Holocene. These findings are robust across multiple plant wax chain lengths (Fig. S4), reinforcing $\delta^2\text{H}_{\text{precip}}$ as the primary driver of $\delta^2\text{H}_{\text{wax}}$ in our samples.

Pollen data further supports our $\delta^2\text{H}_{\text{precip}}$ interpretations. Today, Nuku Hiva’s native cloud forest, found at elevations above 900 m, receives substantial rainfall (>3000 mm/year³³), while herbaceous plants are associated with lower, drier elevations³⁴. In our peat core sediment samples (50 ka–present), the proportion of cloud forest pollen serves as a proxy for past vegetation composition and, by extension, precipitation and temperature changes. The position of this cloud forest is controlled by the competing effects of temperature and precipitation. Cooler temperatures will lower the cloud

forest belt (Lifting Condensation Level), while drier conditions will raise it. Our results show that cloud forest vegetation was least abundant during the last glacial period (Marine Isotope Stage 3–2) (Fig. 2b), with increased proportions of herbaceous taxa (Fig. 2a), before transitioning to increased cloud forest pollen and reduced herbaceous taxa in the early/mid-Holocene. This suggests that during the cool glacial period, the effect of substantially reduced precipitation was the dominant control, forcing the cloud forest to a higher altitude above our study site. During the Early to Mid-Holocene, increased precipitation (Fig. 2c) and relatively cooler temperatures (Fig. 2d) maintained a lower cloud base, facilitating the expansion of the cloud forest. In the Late Holocene, a reduction in precipitation relative to the mid-Holocene maximum, combined with warmer temperatures, likely raised the cloud base, consistent with the observed decrease in cloud forest taxa (Fig. 2b).

Although no other continuous Pleistocene–Holocene precipitation records for the SPCZ exist, the absence of peat formation in nearby Tahiti³⁵ (600 km south of Nuku Hiva) since 38 ka has been interpreted as evidence of cooler, drier conditions, aligning with our reconstructed precipitation patterns based on plant wax and pollen proxies.

brGDGT temperature reconstruction

The methylation of bacterial-derived branched glycerol dialkyl glycerol tetraethers is captured via the MBT'_{5ME} index (see Equation 4 in Methods) and displays a linear relationship with air temperature in a global peat and soil dataset^{36–39}. In our site, core-top brGDGT temperatures (23.2°C) are consistent (i.e., within calibration error) to the mean annual temperature of the To'ovi'i plateau (20.5°C⁴⁰) which gives confidence in the down-core temperature reconstruction. Over the past 45 ka, we observe a notably large 9°C range in reconstructed temperatures (Fig. 2d). Temperatures during 45–35 ka remained relatively stable between 16–18°C, before cooling to a broad minimum of 13–14°C during 32–24 ka. The temperature minimum in our record occurs at ~23 ka, slightly earlier than the global Last Glacial Maximum (19–21 ka). This early cooling is consistent with records of tropical glacier advances⁴¹. Although Nuku Hiva remained unglaciated, this synchrony indicates a coherent, pan-tropical atmospheric cooling signal that simultaneously lowered the freezing level at high elevations and reduced ambient air temperatures at our study site. Warming began at 23 ka, rising by 9°C to reach a maximum of 22–23°C in the late Holocene. Interestingly, the range in temperatures reconstructed from our Nuku Hiva core is much larger than the changes seen in tropical SST (2–5°C) obtained via data assimilation reconstructions, a technique that blends model and proxy data e.g.^{42;43}. However, Glacial-age reconstructions (Marine Isotope Stage 2) from Hawaii and Papua New Guinea indicate that temperatures were 7°C and 6°C, respectively, cooler than preindustrial levels^{44;45}. Similarly, brGDGT reconstructions of lake temperatures from Indonesia and eastern Africa reveal maximum temperature decreases of 9°C and 5.5°C, respectively, relative to

preindustrial conditions during the last glacial maximum^{46;47}. While lower sea levels and changes in the adiabatic gradient⁴⁷ may have amplified terrestrial cooling compared to SST cooling during the last glacial period, the greater magnitude of cooling observed at tropical terrestrial sites, including our Nuku Hiva site, is nevertheless difficult to reconcile with the relatively smaller cooling seen in SST.

Cooler and drier during the glacial period

$\delta^2\text{H}_{\text{precip}}$ and brGDGT temperature, both reconstructed from our Nuku Hiva core sediments, are negatively correlated during glacial conditions (Fig. 3). This correlation is present between $\delta^2\text{H}_{\text{precip}}$ reconstructed from long chain *n*-alkanes ($\delta^2\text{H}_{\text{precip(alkane)}}$) and long/short-chain *n*-alkanoic acids ($\delta^2\text{H}_{\text{precip(acid)}}$) (Fig. S3), indicating that the signal is broadly robust to changes in plant types and/or aquatic inputs. This relationship implies that warmer conditions are strongly related to wetter conditions in Nuku Hiva over the past 50 ka. We note that some Holocene $\delta^2\text{H}_{\text{precip}}$ and brGDGT temperature data do not follow the linear relationship present in the glacial period (Fig. 3), with $\delta^2\text{H}_{\text{precip}}$ appearing more negative than the glacial trend would predict.

To investigate whether this offset resulted from ecological shifts, specifically the expansion of arboreal taxa during the Holocene, we applied a dynamic vegetation correction weighted by pollen abundance (see Methods). While pollen assemblages indicate substantial community turnover - characterised by a $\sim 20\%$ increase in woody taxa from the Glacial to the Holocene - our sensitivity analysis demonstrates that the net impact on the reconstructed isotope record is minor (Supplementary Information). This stability arises because the biosynthetic fractionation factors of the dominant functional types (trees, herbs, and ferns) broadly overlap, resulting in a relatively stable landscape-integrated fractionation factor over time. Consequently, the vegetation correction confirms that the observed variance in $\delta^2\text{H}_{\text{wax}}$ is primarily driven by hydrological changes rather than vegetation succession, validating the strong coupling between cooler temperatures and reduced precipitation during the glacial period.

Previous modelling work has demonstrated that the mean state temperature of the Pacific Ocean exerts a significant control on both the strength and location of the SPCZ⁴⁸, with a 4°C SST cooling resulting in a 20% decrease in precipitation due to lower atmospheric moisture content and reduced atmospheric convection. Thus this thermodynamic change likely played a large role in reducing precipitation to Nuku Hiva during the glacial period, as evidenced by the moderate correlation ($r = 0.50$, $p < 0.01$) between temperature and precipitation in our proxy reconstructions (Fig. 3). However, in the modern era, precipitation at Nuku Hiva is also strongly related to indices of zonal temperature gradients¹², which convolves the dynamic and thermodynamic influences on precipitation. We therefore must consider the influence of dynamic changes in atmospheric circulation patterns on the

SPCZ location, especially in light of the sensitivity of Nuku Hiva precipitation to zonal SPCZ events (Fig. S1).

Modelling studies and data assimilations do not provide a consistent direction of precipitation change in Nuku Hiva during the last glacial period, limiting their use in determining larger atmospheric circulation changes. For example, the Paleoclimate Modelling Intercomparison Project phase 4 (PMIP4) – that is Palaeoclimate simulations run using CMIP6 models – ensemble mean⁴⁹ suggests that Nuku Hiva experienced wetter conditions during the LGM, with a stronger zonal SPCZ (Fig. 4b). By considering the response to individual models (Fig. 4c–f) we see that this wetting signal is largely due to a combination of a more northeastward SPCZ position (particularly Fig. 4c,f) and an intensification of the “double-ITCZ” bias^{50–54} (especially clear in Fig. 4d). In contrast, the LGM 2020 data assimilation with iCESM1.2/2⁴² indicates a drier eastern SPCZ (Fig. 4a). This discrepancy may be partly attributed to model biases, particularly in representing the eastern Pacific cold tongue, which influences the modern position of the SPCZ². The “double-ITCZ” bias is visible in the LGM2020 data assimilation (see black contours in Fig. 4a), likely due to the use of coupled model data in the assimilation process, however the bias is weakened here rather than strengthened (as is seen in Fig. 4b–f).

Whilst more research is needed to resolve the complex interactions between the SPCZ, SST distributions, and ocean circulation patterns during the glacial period, these early findings indicate that precipitation decreased relative to preindustrial conditions during the glacial period in Nuku Hiva, which is broadly consistent with a reduction of atmospheric moisture due to cooler air temperatures. The spread in model and assimilation responses to LGM changes in this region further emphasizes the need for long-term proxy records to complement and refine model simulations of this time period. This study provides the first proxy-based confirmation of a strong positive correlation between temperature and precipitation in the eastern SPCZ and offers the first terrestrial record indicating cooler, drier conditions in the SPCZ during the late glacial period.

Methods

Sediment core and chronology

We collected duplicate peat cores (NHS-2A and NHS-2B) using a Russian Corer from Moūku Swamp (8.869°S, 140.138°W, 850 m asl) on the To'ovi'i plateau, Nuku Hiva, French Polynesia (Fig. 1). This 400×50 m ribbon swamp is sustained by groundwater inflow and rainfall. Both cores were correlated by aligning separate core segments using elemental data derived from X-ray fluorescence analysis. NHS-2A was sampled for radiocarbon, biomarkers and pollen, whilst NHS-2B was kept as a reference archive. After collection, cores were transported to the University of Southampton Department of Geography and were kept refrigerated at 5°C. To generate an age model, we obtained 15 ¹⁴C dates from both plant macro-fossils and bulk sediments from the NHS-2A core and then used the Bayesian r package BACON⁶⁹ to generate an ensemble of age–depth models. Average 1- σ uncertainty was relatively low (0.4 ka) between 26–0 ka but increased between 60–26 ka (1.8 ka).

Lipid extraction

Biomarker samples (3–6 g) were processed by drying, grinding, and extraction using a Dionex Accelerated Solvent Extraction system at the University of Southampton. The extraction was performed with a solvent mixture of 9:1 dichloromethane (DCM) to methanol (MeOH) at 100°C and a pressure of 1,500 psi to obtain the Total Lipid Extract (TLE). The TLEs were further separated into neutral and acid fractions using NH₂ sepra bulk packing columns. The neutral fraction was eluted with a 2:1 mixture of DCM to isopropanol, while the acid fraction was eluted with 4% acetic acid (CH₃COOH) in DCM.

The neutral fraction underwent additional separation using columns packed with silica gel. The *n*-alkanes were eluted using hexane, and the polar fraction was eluted with DCM followed by methanol. To prepare for Gas Chromatograph (GC) analyses, *n*-alkanes were treated with copper to remove any elemental sulphur. Fatty acids were converted to fatty acid methyl esters (FAMES) by methylation using a 95:5 mixture of MeOH to hydrochloric acid at 70°C for 12 hours. The methanol used had a known isotopic composition with a methyl group $\delta^2\text{H}$ of -179‰ . Both *n*-alkanes and *n*-alkanoic were identified and quantified using Gas Chromatography (Thermo Trace 1310, column dimension 60 m) with a Flame Ionization Detector (GC-FID) and through comparison with an in-house standard containing known concentrations of *n*-alkanoic acids and *n*-alkanes.

Lipid distribution

Carbon preference index (CPI) Equation 1 and average chain length (ACL) Equation 2 were calculated to represent chain length distributions by

$$CPI = \frac{2[C_n]}{[C_{n-1}] + [C_{n+1}]}, \quad (1)$$

$$ACL = \frac{\sum (n \times [C_n])}{\sum [C_n]}, \quad (2)$$

where C_n , refers to the n -alkane or n -alkanoic acid of length n (for C_{27} to C_{31} n -alkanes, and C_{24} to C_{30} n -alkanoic acids).

Lipid Hydrogen isotope analysis

To reconstruct past trends in hydroclimate we measured the hydrogen isotopic composition of plant wax (δ^2H_{wax}), n -alkanoic acids (C_{22} , C_{24} , C_{26} , C_{28} and C_{30}) and n -alkanes (C_{27} and C_{29}). The interpretation of δ^2H_{wax} is based on its relationship with both the isotopic value of source water (precipitation) and the physiological effects of evapotranspiration. Drier and/or less humid conditions lead to higher δ^2H_{wax} values due to a combination of less rainout (the ‘amount effect’) and greater evaporative enrichment of deuterium in leaf water²².

The δ^2H_{wax} values were measured using a Thermo Trace 1310 system with a Restek column ($30\text{ m} \times 0.25\text{ mm} \times 0.1\text{ }\mu\text{m}$) coupled to a Thermo Scientific Delta V Plus isotope ratio mass spectrometer via GC Isolink with pyrolysis furnace (1400°C) at the University of Southampton. Linearity in δ^2H measurements was monitored daily using H_2 reference gas, with a mean H^+ factor of (2.59 ppm/mV) recorded. A standard containing C_{17} – C_{25} n -alkanes with known isotopic compositions (A6 mix supplied by A. Schimmelmann, University of Indiana, with δ^2H values from -17 to -256‰) was measured daily with mean RMS of 1.7‰. This allowed for the normalization to Vienna Standard Mean Ocean Water and Vienna Pee Dee Belemnite, respectively. The reported δ^2H_{wax} values for n -alkanoic acids were corrected to account for the methyl group’s H contribution.

Hydroclimate Reconstruction and Vegetation Correction

To decouple the source water hydrogen isotope composition (δ^2H_{water}) from the sedimentary leaf wax record (δ^2H_{wax}), we applied a time-variable correction for apparent fractionation driven by vegetation turnover. Building on the theoretical and empirical foundation established by previous studies^{28–30}, we accounted for the distinct biosynthetic fractionation factors exerted by different plant functional

types. Specifically we employed a linear mixing model weighted by the relative abundance of pollen taxa to calculate the net fractionation factor (ϵ_{mix}) at each time step:

$$\epsilon_{mix}(t) = [f_{tree}(t) \cdot \epsilon_{tree}] + [f_{herb}(t) \cdot \epsilon_{herb}] + [f_{fern}(t) \cdot \epsilon_{fern}], \quad (3)$$

where f represents the fractional abundance of pollen for Trees, Herbs, and Ferns, derived from the interpolated pollen record.

End-member fractionation factors were defined using a compilation of published $\delta^2\text{H}_{wax}$ data from modern plants, prioritising tropical environments to reflect the study region. The fractionation factor for trees was derived from tropical tree-derived leaf waxes^{26;70–72}, yielding a mean ϵ_{tree} of $-129 \pm 3\text{‰}$ (1 standard error of the mean; SEM). The herbaceous end-member was defined using tropical herb and grass data^{70–73}, resulting in a mean ϵ_{herb} of $-133 \pm 7\text{‰}$ (1 SEM). Due to the scarcity of compound-specific hydrogen isotope data for tropical ferns, we utilized a global compilation of fern leaf waxes^{27;73–75}, yielding a mean ϵ_{fern} of $-113 \pm 5\text{‰}$ (1 SEM).

Uncertainty was propagated via a Monte Carlo simulation ($n = 4,000$). We accounted for three distinct sources of error: (1) chronological uncertainty, utilizing the ensemble of age models generated for the core; (2) analytical uncertainty, modeled as random Gaussian noise based on the instrumental error ($1\sigma = 2\text{‰}$); and (3) calibration uncertainty. For the latter, ϵ values for each functional type were randomly sampled in each iteration from normal distributions defined by the SEM of the respective calibration datasets. We utilized the SEM rather than the standard deviation to reflect the catchment-integrated nature of the sedimentary signal, which represents an average of the regional vegetation population rather than individual plant variability. Changes in global ice volume were corrected prior to the vegetation correction using standard benthic $\delta^{18}\text{O}$ stacks interpolated to the age ensemble. Final $\delta^2\text{H}_{water}$ time series are presented as the mean of the Monte Carlo simulations, with error envelopes representing the 1σ and 2σ confidence intervals.

GDGT analysis

The neutral polar fraction was analysed at the University of Southampton using an Agilent 1260 High-Performance Liquid Chromatography system coupled with an Agilent 6120 mass spectrometer (MS), following the methodology described by Hopmans et al. (2016) with compounds detected using the single ion monitoring mode. We calculated the temperature sensitive 5-methyl brGDGT index^{38;76}, $\text{MBT}'_{5\text{ME}}$, as

$$\text{MBT}'_{5\text{ME}} = \frac{(Ia + Ib + Ic)}{(Ia + Ib + Ic + IIa + IIb + IIc + IIIa)} \quad (4)$$

where type I, II, and III brGDGTs are characterized by four, five, and six methyl groups, respectively, whereas type a, b, and c brGDGTs are distinguished by having zero, one, and two cyclopentane moieties, respectively.

Throughout the runs, analyses of an internal laboratory standard and duplicate analyses indicated an error of 0.009 $\text{MBT}'_{5\text{ME}}$ units (1σ). Different environmental settings (e.g. lakes vs soils/peats) have a different relationship between $\text{MBT}'_{5\text{ME}}$ and temperature and thus may require a different core-top calibration e.g. ^{38;39}. In order to constrain the sources of brGDGT to our sediment core, we applied the machine learning “BIGMaC” model⁷⁷ to identify brGDGT sources based on the distribution of isoprenoid and brGDGTs. We find that GDGTs in all samples are derived from bacteria living in a peat environment, enabling the conversion of $\text{MBT}'_{5\text{ME}}$ to temperature using the soil/peat calibration model BayMBT_0 ³⁶ which has a mean root mean squared error of 4°C.

Acknowledgements. We are grateful for the help and support offered by the Délégation à la Recherche de la Polynésie française. We thank the mayor of Nuku Hiva, and the Department of Agriculture in Nuku Hiva for thoughtful discussions related to this work. We thank William Roberts and PROMS project partners for thoughtful discussions related to this study. This study was supported by NERC grant NE/W005565/1 to DAS and MJ. Field work and some radiocarbon dates were funded by National Geographic Society project NGS-58688R-19 “Chasing the Rain” awarded to DAS. GNI was supported by a Royal Society Dorothy Hodgkin Fellowship (DHF\R1\191178 and DHF\R\241007). Thanks to Ministère De L’Agriculture, Du Foncier, Gov. of French Polynesia and to Délégation à la Recherche de la Polynésie française, Dr Jean-Yves Meyer, for permission to undertake the sampling and return of samples under UK Gov. FERA Licence.

Data Availability

Proxy data generated as part of this study are available via Zenodo⁷⁸.

Competing interests

The authors declare no competing interests.

Contributions

All authors contributed to the conceptualisation of the study. D.S. supervised the project. M.P. performed data acquisition and analysis, curated the data, and led the writing of the paper. D.T.S. contributed to data acquisition and analysis and writing of the paper. D.S., P.L., M.J., and T.J.O., R.S and J.Y.M also contributed to data acquisition. Funding for the project was acquired by D.S.,

G.N.I., M.J., P.L., A.J.M., and T.J.O. All authors contributed to the editing and review of the final manuscript.

References

- [1] Power, S. B., Schiller, A., Cambers, G., Jones, D. & Hennessy, K. The Pacific climate change science program. *Bulletin of the American Meteorological Society* **92**, 1409–1411 (2011). URL <http://www.jstor.org/stable/26218598>.
- [2] Brown, J. R. *et al.* South Pacific Convergence Zone dynamics, variability and impacts in a changing climate. *Nature Reviews Earth & Environment* **1**, 530–543 (2020). URL <https://doi.org/10.1038/s43017-020-0078-2>.
- [3] Vincent, E. M. *et al.* Interannual variability of the South Pacific Convergence Zone and implications for tropical cyclone genesis. *Climate dynamics* **36**, 1881–1896 (2011). URL <https://doi.org/10.1007/s00382-009-0716-3>.
- [4] Salinger, M., Renwick, J. A. & Mullan, A. Interdecadal Pacific Oscillation and South Pacific climate. *International journal of climatology: a journal of the Royal Meteorological Society* **21**, 1705–1721 (2001). URL <https://doi.org/10.1002/joc.691>.
- [5] Brown, J., Moise, A. & Colman, R. The South Pacific Convergence Zone in CMIP5 simulations of historical and future climate. *Climate Dynamics* **41**, 2179–2197 (2013). URL <https://doi.org/10.1007/s00382-012-1591-x>.
- [6] Cai, W. *et al.* More extreme swings of the South Pacific convergence zone due to greenhouse warming. *Nature* **488**, 365–369 (2012). URL <https://doi.org/10.1038/nature11358>.
- [7] Linsley, B. K. *et al.* SPCZ zonal events and downstream influence on surface ocean conditions in the Indonesian Throughflow region. *Geophysical Research Letters* **44**, 293–303 (2017). URL <https://doi.org/10.1002/2016GL070985>.
- [8] d’Aubert, A. & Nunn, P. D. *Furious Winds and Parched Islands: Tropical Cyclones (1558–1970) and Droughts* (Xlibris Corporation, United States, 2012).
- [9] Faraji, M. *et al.* High-resolution reconstruction of infiltration in the Southern Cook Islands based on trace elements in speleothems. *Quaternary Research* **118**, 20–40 (2024). URL <https://doi.org/10.1017/qua.2023.51>.

- [10] Faraji, M. et al. Controls on rainfall variability in the tropical South Pacific for the last 350 years reconstructed from oxygen isotopes in stalagmites from the Cook Islands. Quaternary Science Reviews **289**, 107633 (2022). URL <https://doi.org/10.1016/j.quascirev.2022.107633>.
- [11] Maupin, C. et al. Persistent decadal-scale rainfall variability in the tropical South Pacific Convergence Zone through the past six centuries. Climate of the Past **10**, 1319–1332 (2014). URL <https://doi.org/10.5194/cp-10-1319-2014>.
- [12] Peuple, M. et al. Ocean variability drives a millennial-scale shift in South Pacific hydroclimate. Communications Earth & Environment (2025). URL <https://doi.org/10.1038/s43247-025-02676-5>.
- [13] Brown, J. R., Moise, A. F. & Delage, F. P. Changes in the South Pacific Convergence Zone in IPCC AR4 future climate projections. Climate dynamics **39**, 1–19 (2012). URL <https://doi.org/10.1007/s00382-011-1192-0>.
- [14] Narsey, S. et al. Storylines of South Pacific Convergence Zone changes in a warmer world. Journal of Climate **35**, 6549 – 6567 (2022). URL <https://doi.org/10.1175/JCLI-D-21-0433.1>.
- [15] Saint-Lu, M., Braconnot, P., Leloup, J., Lengaigne, M. & Marti, O. Changes in the ENSO/SPCZ relationship from past to future climates. Earth and Planetary Science Letters **412**, 18–24 (2015). URL <https://doi.org/10.1016/j.epsl.2014.12.033>.
- [16] Widlansky, M. J. et al. Changes in South Pacific rainfall bands in a warming climate. Nature climate change **3**, 417–423 (2013). URL <https://doi.org/10.1038/nclimate1726>.
- [17] Maloney, A. E. et al. Contrasting Common Era climate and hydrology sensitivities from paired lake sediment dinosterol hydrogen isotope records in the South Pacific Convergence Zone. Quaternary Science Reviews **281**, 107421 (2022). URL <https://doi.org/10.1016/j.quascirev.2022.107421>.
- [18] Sear, D. A. et al. Human settlement of East Polynesia earlier, incremental, and coincident with prolonged South Pacific drought. Proceedings of the National Academy of Sciences **117**, 8813–8819 (2020). URL <https://doi.org/10.1073/pnas.1920975117>.
- [19] Toomey, M. R., Donnelly, J. P. & Tierney, J. E. South Pacific hydrologic and cyclone variability during the last 3000 years. Paleoceanography **31**, 491–504 (2016). URL <https://doi.org/10.1002/2015PA002870>.

- [20] Adler, R. F. et al. The Global Precipitation Climatology Project (GPCP) monthly analysis (new version 2.3) and a review of 2017 global precipitation. Atmosphere **9**, 138 (2018). URL <https://doi.org/10.3390/atmos9040138>.
- [21] McGee, D. Glacial–Interglacial precipitation changes. Annual Review of Marine Science **12**, 525–557 (2020). URL <https://doi.org/10.1146/annurev-marine-010419-010859>.
- [22] Sachse, D. et al. Molecular paleohydrology: interpreting the hydrogen-isotopic composition of lipid biomarkers from photosynthesizing organisms. Annual Review of Earth and Planetary Sciences **40**, 221–249 (2012). URL <https://doi.org/10.1146/annurev-earth-042711-105535>.
- [23] Ladd, S. N. et al. Leaf wax hydrogen isotopes as a hydroclimate proxy in the tropical Pacific. Journal of Geophysical Research: Biogeosciences **126**, e2020JG005891 (2021). URL <https://doi.org/10.1029/2020JG005891>.
- [24] McFarlin, J. M., Axford, Y., Masterson, A. L. & Osburn, M. R. Calibration of modern sedimentary $\delta^{2}\text{H}$ plant wax-water relationships in Greenland lakes. Quaternary Science Reviews **225**, 105978 (2019). URL <https://doi.org/10.1016/j.quascirev.2019.105978>.
- [25] Maloney, A. E. et al. Reconstructing precipitation in the tropical South Pacific from dinosterol 2H/1H ratios in lake sediment. Geochimica et Cosmochimica Acta **245**, 190–206 (2019). URL <https://doi.org/10.1016/j.gca.2018.10.029>.
- [26] Feakins, S. J. et al. Plant leaf wax biomarkers capture gradients in hydrogen isotopes of precipitation from the Andes and Amazon. Geochimica et Cosmochimica Acta **182**, 155–172 (2016). URL <https://doi.org/10.1016/j.gca.2016.03.018>.
- [27] Hou, J., D’Andrea, W. J., MacDonald, D. & Huang, Y. Hydrogen isotopic variability in leaf waxes among terrestrial and aquatic plants around Blood Pond, Massachusetts (USA). Organic Geochemistry **38**, 977–984 (2007). URL <https://doi.org/10.1016/j.orggeochem.2006.12.009>.
- [28] Feakins, S. J. Pollen-corrected leaf wax D/H reconstructions of northeast African hydrological changes during the late Miocene. Palaeogeography, Palaeoclimatology, Palaeoecology **374**, 62–71 (2013). URL <https://doi.org/10.1016/j.palaeo.2013.01.004>.
- [29] Konecky, B. et al. WaxPSM: A forward model of leaf wax hydrogen isotope ratios to bridge proxy and model estimates of past climate. Journal of Geophysical Research: Biogeosciences

124, 2107–2125 (2019). URL <https://doi.org/10.1029/2018JG004708>.

- [30] Yang, D. & Bowen, G. J. Integrating plant wax abundance and isotopes for paleo-vegetation and paleoclimate reconstructions: a multi-source mixing model using a Bayesian framework. *Climate of the Past* **18**, 2181–2210 (2022). URL <https://doi.org/10.5194/cp-18-2181-2022>.
- [31] Lisiecki, L. E. & Stern, J. V. Regional and global benthic $\delta^{18}\text{O}$ stacks for the last glacial cycle. *Paleoceanography* **31**, 1368–1394 (2016). URL <https://doi.org/10.1002/2016PA003002>.
- [32] Dongmann, G., Nürnberg, H., Förstel, H. & Wagener, K. On the enrichment of H_2^{18}O in the leaves of transpiring plants. *Radiation and environmental biophysics* **11**, 41–52 (1974). URL <https://doi.org/10.1007/BF01323099>.
- [33] Meyer, J. *Montane cloud forests on remote islands of Oceania: the example of French Polynesia (South Pacific Oceania)* 121–129 (Cambridge University Press, 2010). URL <https://doi.org/10.1017/CBO9780511778384.012>.
- [34] Florence, J. & Lorence, D. H. Introduction to the flora and vegetation of the Marquesas Islands. *Allertonia* 226–237 (1997). URL <https://www.jstor.org/stable/23190456>.
- [35] Prebble, M. *et al.* Abrupt late Pleistocene ecological and climate change on Tahiti (French Polynesia). *Journal of Biogeography* **43**, 2438–2453 (2016). URL <https://doi.org/10.1111/jbi.12807>.
- [36] Crampton-Flood, E. D., Tierney, J. E., Peterse, F., Kirkels, F. M. & Damsté, J. S. S. BayMBT: A bayesian calibration model for branched glycerol dialkyl glycerol tetraethers in soils and peats. *Geochimica et Cosmochimica Acta* **268**, 142–159 (2020). URL <https://doi.org/10.1016/j.gca.2019.09.043>.
- [37] Weijers, J. W., Schouten, S., van den Donker, J. C., Hopmans, E. C. & Damsté, J. S. S. Environmental controls on bacterial tetraether membrane lipid distribution in soils. *Geochimica et Cosmochimica Acta* **71**, 703–713 (2007). URL <https://doi.org/10.1016/j.gca.2006.10.003>.
- [38] Jonge, C. D. *et al.* Occurrence and abundance of 6-methyl branched glycerol dialkyl glycerol tetraethers in soils: Implications for palaeoclimate reconstruction. *Geochimica et Cosmochimica Acta* **141**, 97–112 (2014). URL <https://doi.org/10.1016/j.gca.2014.06.013>.

- [39] Naafs, B. D. A. et al. Introducing global peat-specific temperature and pH calibrations based on brGDGT bacterial lipids. *Geochimica et Cosmochimica Acta* **208**, 285–301 (2017). URL <https://doi.org/10.1016/j.gca.2017.01.038>.
- [40] Laurent, V. & Maamaatuaiahutapu, K. *Atlas climatologique de la Polynésie française* (Météo-France, Direction interrégionale de Polynésie française, Faa'a, Tahiti, Polynésie française, 2019).
- [41] Shakun, J. D. et al. Regional and global forcing of glacier retreat during the last deglaciation. *Nature Communications* **6**, 1–7 (2015). URL <https://doi.org/10.1038/ncomms9059>.
- [42] Tierney, J. E. et al. Glacial cooling and climate sensitivity revisited. *Nature* **584**, 569–573 (2020). URL <https://doi.org/10.1038/s41586-020-2617-x>.
- [43] Annan, J. D., Hargreaves, J. C. & Mauritsen, T. A new global surface temperature reconstruction for the Last Glacial Maximum. *Climate of the Past* **18**, 1883–1896 (2022). URL <https://doi.org/10.5194/cp-18-1883-2022>.
- [44] Blard, P.-H., Lavé, J., Pik, R., Wagnon, P. & Bourlès, D. Persistence of full glacial conditions in the central Pacific until 15,000 years ago. *Nature* **449**, 591–594 (2007). URL <https://doi.org/10.1038/nature06142>.
- [45] Barrows, T. T., Hope, G. S., Prentice, M. L., Fifield, L. K. & Tims, S. G. Late Pleistocene glaciation of the Mt Giluwe volcano, Papua New Guinea. *Quaternary Science Reviews* **30**, 2676–2689 (2011). URL <https://doi.org/10.1016/j.quascirev.2011.05.022>.
- [46] Zhao, B. et al. Evaluating global temperature calibrations for lacustrine branched GDGTs: Seasonal variability, paleoclimate implications, and future directions. *Quaternary Science Reviews* **310**, 108124 (2023). URL <https://doi.org/10.1016/j.quascirev.2023.108124>.
- [47] Loomis, S. E. et al. The tropical lapse rate steepened during the Last Glacial Maximum. *Science Advances* **3**, e1600815 (2017). URL <https://doi.org/10.1126/sciadv.1600815>.
- [48] van der Wiel, K., Matthews, A. J., Joshi, M. M. & Stevens, D. P. Why the South Pacific Convergence Zone is diagonal. *Climate Dynamics* **46**, 1683–1698 (2016). URL <https://doi.org/10.1007/s00382-015-2668-0>.
- [49] Kageyama, M. et al. The PMIP4-CMIP6 Last Glacial Maximum experiments: preliminary results and comparison with the PMIP3-CMIP5 simulations. *Climate of the Past Discussions* **2020**, 1–37 (2020). URL <https://doi.org/10.5194/cp-17-1065-2021>.

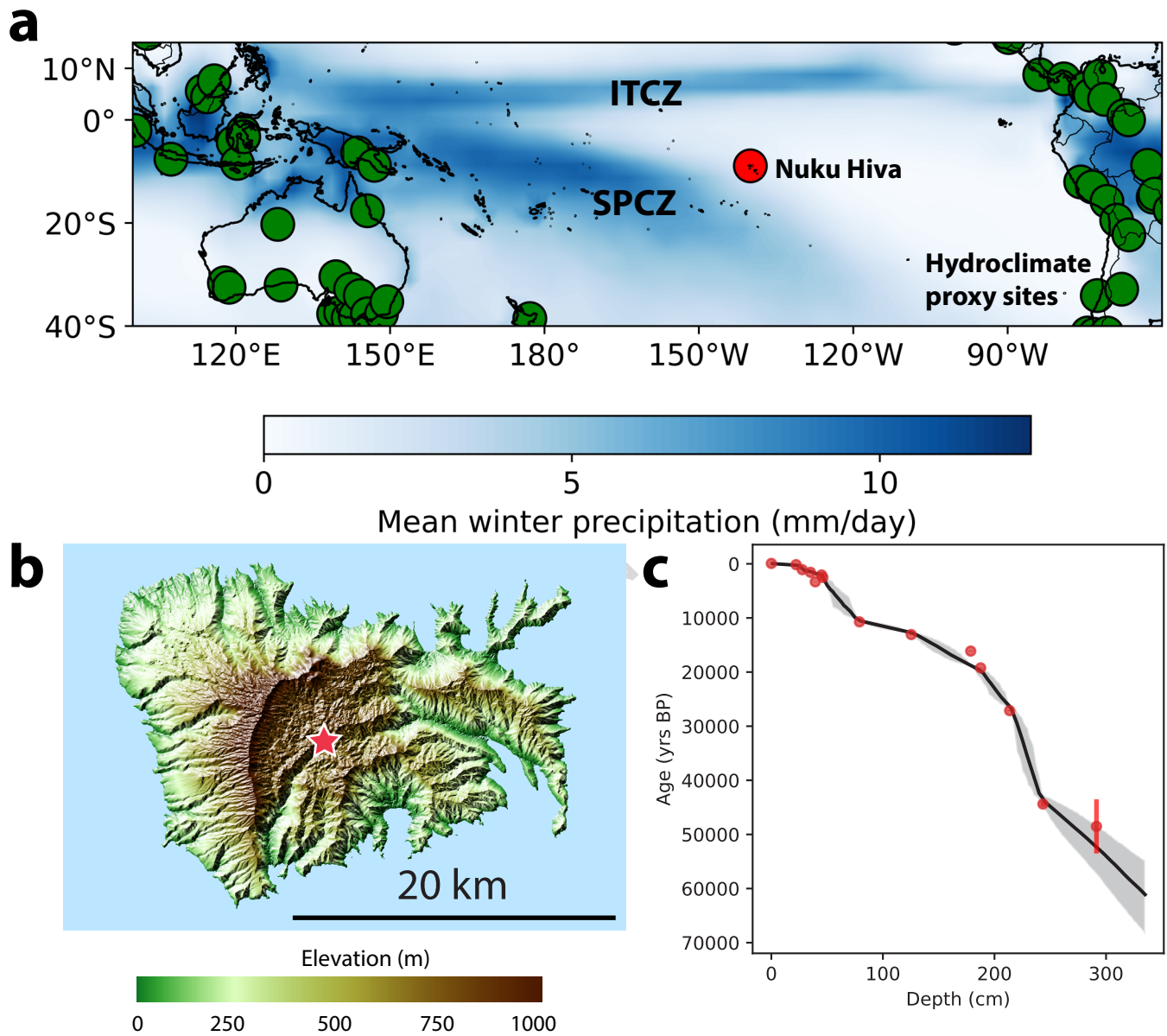
- [50] Li, Z. & Fedorov, A. T. Climate Models Exaggerate the Enhanced Double-ITCZ in the Warming Tropical Pacific Due To Preexisting Precipitation Bias. Geophysical Research Letters **52**, e2025GL115445 (2025). URL <https://doi.org/10.1029/2025GL115445>.
- [51] Tian, B. & Dong, X. The Double-ITCZ Bias in CMIP3, CMIP5, and CMIP6 Models Based on Annual Mean Precipitation. Geophysical Research Letters **47**, e2020GL087232 (2020). URL <https://doi.org/10.1029/2020GL087232>.
- [52] Li, G. & Xie, S.-P. Tropical biases in CMIP5 multimodel ensemble: The excessive equatorial pacific cold tongue and double ITCZ problems. Journal of Climate **27**, 1765 – 1780 (2014). URL <https://doi.org/10.1175/JCLI-D-13-00337.1>.
- [53] Samanta, D., Karnauskas, K. B. & Goodkin, N. F. Tropical Pacific SST and ITCZ biases in climate models: Double trouble for future rainfall projections? Geophysical Research Letters **46**, 2242–2252 (2019). URL <https://doi.org/10.1029/2018GL081363>.
- [54] Fiedler, S. et al. Simulated tropical precipitation assessed across three major phases of the Coupled Model Intercomparison Project (CMIP). Monthly Weather Review **148**, 3653–3680 (2020). URL <https://doi.org/10.1175/MWR-D-19-0404.1>.
- [55] Shi, X., Yang, H., Danek, C. & Lohmann, G. AWI AWI-ESM1.1LR model output prepared for CMIP6 PMIP lgm, version 20200212. Earth System Grid Federation (2020). URL <https://doi.org/10.22033/ESGF/CMIP6.9330>.
- [56] Danek, C. et al. AWI AWI-ESM1.1LR model output prepared for CMIP6 CMIP piControl, version v20200212. Earth System Grid Federation (2020). URL <https://doi.org/10.22033/ESGF/CMIP6.9335>.
- [57] Shi, X., Werner, M., Wang, Q., Yang, H. & Lohmann, G. Simulated mid-holocene and last interglacial climate using two generations of AWI-ESM. Journal of Climate **35**, 7811 – 7831 (2022). URL <https://doi.org/10.1175/JCLI-D-22-0354.1>.
- [58] Volodin, E. et al. INM INM-CM4-8 model output prepared for CMIP6 PMIP lgm, version 20201112. Earth System Grid Federation (2019). URL <https://doi.org/10.22033/ESGF/CMIP6.5075>.
- [59] Volodin, E. et al. INM INM-CM4-8 model output prepared for CMIP6 CMIP piControl, version 20190605. Earth System Grid Federation (2019). URL <https://doi.org/10.22033/ESGF/CMIP6.5080>.

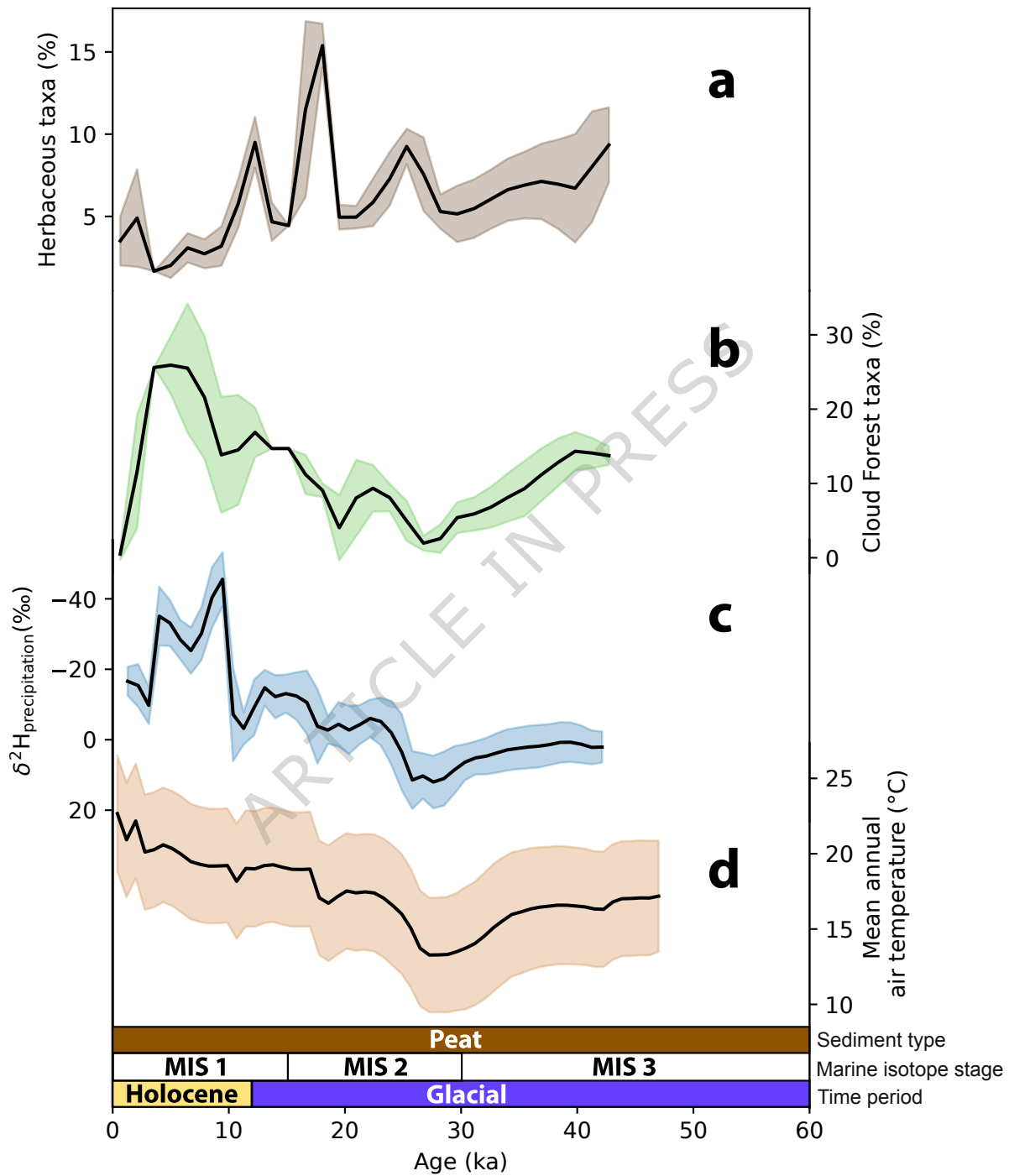
- [60] Volodin, E. M. et al. Simulation of the modern climate using the INM-CM48 climate model. Russian Journal of Numerical Analysis and Mathematical Modelling **33**, 367–374 (2018). URL <https://doi.org/10.1515/rnam-2018-0032>.
- [61] Ohgaito, R. et al. MIROC MIROC-ES2L model output prepared for CMIP6 PMIP lgm, version 20191002. Earth System Grid Federation (2019). URL <https://doi.org/10.22033/ESGF/CMIP6.5644>.
- [62] Hajima, T. et al. MIROC MIROC-ES2L model output prepared for CMIP6 CMIP piControl, version 20190823. Earth System Grid Federation (2019). URL <https://doi.org/10.22033/ESGF/CMIP6.5710>.
- [63] Ohgaito, R. et al. PMIP4 experiments using MIROC-ES2L Earth system model. Geoscientific Model Development **14**, 1195–1217 (2021). URL <https://doi.org/10.5194/gmd-14-1195-2021>.
- [64] Hajima, T. et al. Development of the MIROC-ES2L Earth system model and the evaluation of biogeochemical processes and feedbacks. Geoscientific Model Development **13**, 2197–2244 (2020). URL <https://doi.org/10.5194/gmd-13-2197-2020>.
- [65] Jungclaus, J. et al. MPI-M MPI-ESM1.2-LR model output prepared for CMIP6 PMIP lgm, version 20190710. Earth System Grid Federation (2019). URL <https://doi.org/10.22033/ESGF/CMIP6.6642>.
- [66] Wieners, K.-H. et al. MPI-M MPI-ESM1.2-LR model output prepared for CMIP6 CMIP piControl, version 20190710. Earth System Grid Federation (2019). URL <https://doi.org/10.22033/ESGF/CMIP6.6675>.
- [67] Mauritsen, T. et al. Developments in the MPI-M Earth System Model version 1.2 (MPI-ESM1.2) and its response to increasing CO₂. Journal of Advances in Modeling Earth Systems **11**, 998–1038 (2019). URL <https://doi.org/10.1029/2018MS001400>.
- [68] Mauritsen, T. & Roeckner, E. Tuning the MPI-ESM1.2 global climate model to improve the match with instrumental record warming by lowering its climate sensitivity. Journal of Advances in Modeling Earth Systems **12**, e2019MS002037 (2020). URL <https://doi.org/10.1029/2019MS002037>. E2019MS002037 10.1029/2019MS002037.
- [69] Blaauw, M. & Christen, J. A. Flexible paleoclimate age–depth models using an autoregressive gamma process. Bayesian Analysis **6**, 457–474 (2011). URL <https://doi.org/10.1214/11-BA618>.

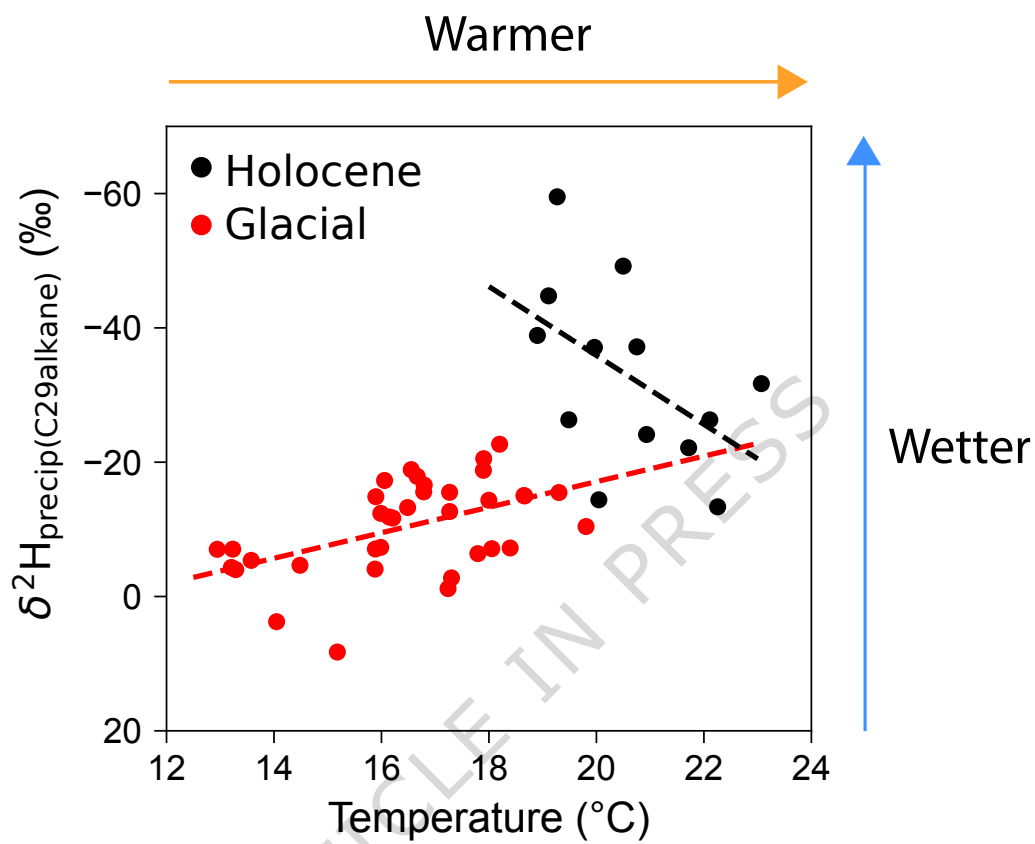
- [70] Bi, X. *et al.* Molecular and carbon and hydrogen isotopic composition of n-alkanes in plant leaf waxes. *Organic Geochemistry* **36**, 1405–1417 (2005). URL <https://doi.org/10.1016/j.orggeochem.2005.06.001>.
- [71] Krull, E. *et al.* Compound-specific $\delta^{13}\text{C}$ and $\delta^2\text{H}$ analyses of plant and soil organic matter: A preliminary assessment of the effects of vegetation change on ecosystem hydrology. *Soil Biology and Biochemistry* **38**, 3211–3221 (2006). URL <https://doi.org/10.1016/j.soilbio.2006.04.008>.
- [72] Liu, W. & Yang, H. Multiple controls for the variability of hydrogen isotopic compositions in higher plant n-alkanes from modern ecosystems. *Global Change Biology* **14**, 2166–2177 (2008). URL <https://doi.org/10.1111/j.1365-2486.2008.01608.x>.
- [73] Chikaraishi, Y. & Naraoka, H. Compound-specific δD – $\delta^{13}\text{C}$ analyses of n-alkanes extracted from terrestrial and aquatic plants. *Phytochemistry* **63**, 361–371 (2003). URL [https://doi.org/10.1016/S0031-9422\(02\)00749-5](https://doi.org/10.1016/S0031-9422(02)00749-5).
- [74] Yao, Y. & Liu, W. Hydrogen isotopic composition of plant leaf wax in response to soil moisture in an arid ecosystem of the northeast Qinghai-Tibetan Plateau, China. *Journal of Arid Land* **9**, 592–600 (2014). URL <https://doi.org/10.1007/s40333-014-0005-9>.
- [75] Ardenghi, N. *et al.* Leaf wax n-alkane distribution and hydrogen isotopic fractionation in fen plant communities of two Mediterranean wetlands (Tenaghi Philippon, Nisi fen—Greece). *Frontiers in Earth Science* **12**, 1359157 (2024). URL <https://doi.org/10.3389/feart.2024.1359157>.
- [76] Hopmans, E. C., Schouten, S. & Damsté, J. S. S. The effect of improved chromatography on GDGT-based palaeoproxies. *Organic Geochemistry* **93**, 1–6 (2016). URL <https://doi.org/10.1016/j.orggeochem.2015.12.006>.
- [77] Martínez-Sosa, P. *et al.* Development and application of the Branched and Isoprenoid GDGT Machine learning Classification algorithm (BIGMaC) for paleoenvironmental reconstruction. *Paleoceanography and Paleoclimatology* **38**, e2023PA004611 (2023). URL <https://doi.org/10.1029/2023PA004611>.
- [78] Peuple, M. Hydroclimate and temperature changes in the eastern SPCZ over the last 55 ka (2025). URL <https://doi.org/10.5281/zenodo.17805719>.

Figure Captions

- Fig. 1: Overview of the Nuku Hiva proxy site.** a) Map of the South Pacific region showing modern mean annual precipitation²⁰ (blue shading), Last Glacial Maximum hydroclimate proxy sites²¹ (green circles) and Nuku Hiva (this study, red circle). b) Topography of Nuku Hiva. Location of study site To'ovi'i plateau) shown by red star. c) Bayesian age–depth model of NHS2-A (this study).
- Fig. 2: Pollen, hydrogen isotope, and reconstructed temperature data derived from our peat sediment core.** a) Herbaceous taxa pollen relative abundance. b) Cloud Forest taxa pollen relative abundance. c) Reconstruction of hydrogen isotopic composition of precipitation using the hydrogen isotope composition of C₂₉-alkane plant wax. d) brGDGT MBT'_{5ME} reconstructed mean annual air temperature using BayMBT₀ (soils) model³⁶. Shading represents 1 standard deviation analytical, calibration and age model uncertainty.
- Fig. 3: Proxy temperature and precipitation reconstruction from Nuku Hiva.** Cross plots of brGDGT temperature reconstruction against a) $\delta^2\text{H}_{\text{precip}(\text{C}29\text{alkane})}$, and b) kernel density estimates of $\delta^2\text{H}_{\text{precip}}$ taking into account age model, analytical and calibration errors (Glacial and Holocene samples are highlighted by red and black markers, respectively.)
- Fig. 4: Comparison of existing LGM precipitation simulations across the South Pacific.** a) Difference in annual mean precipitation (LGM minus late Holocene), from the LGM 2020 data assimilation with iCESM1.2/2⁴². b) PMIP4 multi-model mean difference in annual mean precipitation (LGM minus pre-industrial). c–f) Difference in annual mean precipitation (LGM minus pre-industrial) from PMIP4 models: c) AWI-ESM 1.1 LR^{55–57}, d) INM-CM4-8^{58–60}, e) MIROC-ES2L^{61–64}, f) MPI-ESM1.2^{65–68}. In all panels, black contours show LGM mean precipitation at 2, 4, and 6 mm/day, and Nuku Hiva is marked by a red circle, as in Fig. 1.





a**b**